Manuscript in preparation for ACS Catalysis

Proving a Paradigm in Methanol Steam Reforming: Catalytically Highly Selective In_xPd_y/In_2O_3 Interfaces

Nicolas Köwitsch[1], Lukas Thoni[2], Benjamin Klemmed[2], Albrecht Benad[2], Paul Paciok[3], Marc Heggen[3], Isabel Köwitsch[4], Michael Mehring[4], Alexander Eychmüller[2], Marc Armbrüster[1 *]

[1] *Faculty of Natural Sciences, Institute of Chemistry, Materials for Innovative Energy Concepts, Technische Universität Chemnitz, 09107 Chemnitz, Germany*

[2] *Physical Chemistry, Technische Universität Dresden, Bergstr. 66b, 01062 Dresden, Germany*

[3] *Ernst Ruska-Centrum, Forschungszentrum Jülich, 52425 Jülich, Germany*

[4] *Faculty of Natural Sciences, Institute of Chemistry, Coordination Chemistry, Technische Universität Chemnitz, 09107 Chemnitz, Germany*

* *marc.armbruester@chemie.tu-chemnitz.de*

Keywords

Methanol steam reforming, intermetallic compounds, aerogel, heterogeneous catalysis, PdIn, Pd_2In_3, HR-TEM

Abstract

Methanol steam reforming (MSR) provides clean hydrogen by onboard production, which can directly be used for fuel cell applications – while using appropriate catalysts. In_xPd_y/In_2O_3 aerogels exhibit excellent CO_2-selectivities of 99%. This is caused by the active participation of chemically bound oxygen from the material as proven by isotope-labeled experiments. In addition, the dynamic, temperature-dependent equilibrium between intermetallic and oxidic species has a strong impact on the catalytic properties of the material. Thus, the intermetallic compounds in close proximity to a supporting reducible oxide act as selectivity-decisive redox centers, enabling a Mars-van-Krevelen mechanism, which is responsible for the excellent selectivity towards CO_2.

Introduction

Methanol plays a fundamental role in future energy scenarios, where it serves as hydrogen carrier for energetic purposes and carbon feedstock for the chemical industry.[1,2] Use as energy carrier requires a suitable reaction to convert methanol into hydrogen with the least possible amount of impurities. Particularly, traces of CO are detrimental for the usage of polymer electrolyte membrane fuel cells, requiring CO-levels below 100 ppm.[3] Methanol steam reforming (MSR) is a promising reaction, as the only by-product is CO_2 (eq. 1), which is tolerated by fuel cell catalysts. Side reactions are the methanol decomposition (MD) (eq. 2) and the reverse water gas shift reaction (rWGS) (eq. 3), both resulting in unwanted CO.

$$CH_3OH + H_2O \rightleftharpoons 3\ H_2 + CO_2 \qquad (1)$$

$$CH_3OH \rightleftharpoons 2\ H_2 + CO \qquad (2)$$

$$CO_2 + H_2 \rightleftharpoons H_2O + CO \qquad (3)$$

Catalytic materials for these reactions are commonly Cu-based (e.g. the industrial methanol synthesis catalyst $Cu/ZnO/Al_2O_3$[4–7]) or Pd- or Pt-based systems.[4,8–13] For the latter, an easy-to-reduce support is required to obtain high CO_2-selectivity.[14] Through partial reduction under reaction conditions, intermetallic compounds are formed by reactive metal-support interaction (RMSI),[15] thus showing strongly altered catalytic behavior compared to elemental palladium or platinum.[13,16] In the case of ZnPd/ZnO, it has been shown that the presence of the intermetallic compound alone is insufficient to obtain high CO_2-selectivity, but the additional presence of ZnO is decisive,[17–19] while the intrinsic role of ZnO could not be clarified yet. Nevertheless, the paradigm arose that high CO_2-selectivty requires synergistic effects between intermetallic compounds and supporting oxides at the interface region. This was partly proven by mechanistic studies on different systems[20,21] but the intrinsic influence besides adsorption properties was never fully clarified, e.g. if the catalytic material changes chemically in the catalytic cycle.

Besides the excellent CO_2-selectivity, a high activity and atom-efficiency is of crucial importance for application. To improve the latter properties, aerogels are suitable materials for which several reviews about synthesis and possible applications are available.[22–24] The main benefits of aerogels for heterogeneous catalysis are the high specific surface area combined with an open pore system, enabling an excellent dispersion of the active component and making a higher fraction of active atoms accessible. This enables a better atom-efficiency compared to classically impregnated systems. Previous work demonstrated the high potential of combining

intermetallic compounds and aerogels in the ZnPd/ZnO system, which boosted the activity by a factor of five to 1300 mmol(H_2)/(mmol(Pd)×h) at 300 °C while maintaining the excellent CO_2-selectivity of 96% compared to an impregnated material.[25]

In addition to the Pd-Zn system, the In-Pd system shows excellent catalytic properties in several heterogeneous reactions like MSR[8,26–29], CO_2 hydrogenation[30,31] and carbohydrate (de)hydrogenation.[32–35] As recent publications have shown, the understanding of structure-activity relationships and reaction-condition-induced structural changes[26,31] is essential for the development of optimized, highly selective catalytic materials. The cause of the high versatility of the system has not been exhaustively investigated and is suspected to be linked to the interaction of intermetallic In-Pd compounds and the oxide support material. This makes the system an ideal candidate to investigate catalytic activity of the interface region. Especially, a potential incorporation of chemically bound oxygen of the interface region of In-Pd (i.e. formed by the intermetallic compound and the oxidic support) into the reaction products would proof that the interface region and not the sole intermetallic is responsible for a high CO_2-selectivity, proofing the aforementioned paradigm.

Pd/In_2O_3 aerogels were synthesized via the epoxide route, pioneered by Gash *et al.*[36,37] with *in situ* infiltration and reduction of Pd-precursors.[25] The as-prepared and pre-treated materials were thoroughly characterized to obtain information about morphology by scanning and transmission electron microscopy (SEM, TEM), specific surface area (nitrogen physisorption measurements), Pd-loading by inductively coupled plasma with optical emission spectroscopy (ICP-OES), reduction behavior by differential thermal analysis coupled with thermogravimetry and mass spectrometry (DTA/TGA/MS) and crystalline phases by powder X-ray diffraction (XRD). The pre-treated materials were subjected to MSR conditions and, to correlate the catalytic activity and selectivity with the present crystalline phases, subsequently characterized after each test by XRD. High-resolution transmission electron microscopy (HR-TEM) and high-resolution scanning transmission electron microscopy combined with energy-dispersive X-ray spectroscopy (STEM/EDX) were applied to samples taken at different steps of the catalytic experiment to obtain nano-scale information about the material changes during MSR conditions. On these well-characterized materials, ^{18}O-labeled MSR experiments were conducted to determine the role of chemically bound oxygen.

Results and Discussion

For a direct comparison between aerogel-based materials with conventionally impregnated materials in literature,[26] the aerogel was synthesized with a composition of 8 wt-% Pd/In_2O_3 (by ICP/OES). The relatively high loading eases phase analyses by powder X-ray diffraction. TEM and SEM analysis of the material in the as-prepared state (Figure 1a and Figure S1) reveal an open porous network structure formed out of the primary particles. The particle diameters of the oxidic indium backbone are in the range of 10 – 30 nm (mean diameter 19(5) nm for the aerogel). XRD analysis of the as-prepared material points to the absence of well-defined indium oxide or hydroxide phases (Figure 1b). For correlation of the catalytic properties with the chemical state of the material, it is mandatory to transfer the material into a defined state, i.e. In_xPd_y intermetallic compounds supported on an In_2O_3 aerogel, by appropriate pre-treatment.

The thermal and chemical behavior of the aerogel in different gas atmospheres was investigated by TGA/MS (Figure 1c). Calcination in synthetic air (20% O_2 in He) and subsequent reduction in 5% H_2 in He revealed several processes. During calcination, a two-step total mass loss of 17.4(5) wt-% was observed. The first step, being accompanied by a water signal in the mass spectrometer, is ascribed to adsorbed water. In addition to water, a CO_2-signal is observed for the second mass loss, which is assigned to the oxidation of organic residues from synthesis. The subsequent reduction reveals three processes (**A**-**C**). The first one (**A**) takes place directly after contact of the material with hydrogen and the associated mass loss of 1.2(5) wt-% matches the expected mass loss of 1.2 wt-% for the reduction of PdO to elemental palladium. At 250 °C an additional partial reduction (**B**) reaches its maximum rate accompanied by a water signal and an additional mass loss of 2.0(5) wt-%. This process represents the formation of InPd via partial reduction of In_2O_3 and subsequent RMSI on the aerogel for which an additional mass loss of 1.8% is expected.[26] Starting at 440 °C, a continuous reduction of bulk In_2O_3 (**C**) occurs until the fully metallic state is reached. Based on this data, the material was pre-treated in two steps: first calcination at 300 °C for 1 h and then subsequent reduction at 230 °C for 1 h in 5% H_2, the latter resulting in a mass loss of 4.0(5) wt-% (3.0 wt-% expected for $InPd/In_2O_3$).

XRD after pre-treatment resulted only in the reflections of cubic In_2O_3 and the intermetallic compound InPd (Figure 2a), formed by RMSI of Pd and In_2O_3.[16] The formation temperature of InPd is lowered by 60 °C compared to impregnated materials,[26] caused by the highly defective structure and small particle size of the aerogel. Physisorption measurements revealed

a decrease of the specific surface area from 82 m^2/g for the as-prepared state to 57 m^2/g for the material reduced at 230 °C, indicating ripening of the particles (Figure 2b).

In-line with the BET results, TEM investigations after pre-treatment revealed particles with slightly enlarged diameter (26(6) nm for the oxidic backbone) and smoother surfaces, caused by thermal ripening (Figure 3a). Additional HR-TEM micrographs showed small and well-dispersed InPd particles with diameters <10 nm which are identified via their (100)-spacing of $d = 3.2$ Å on highly crystalline In_2O_3 particles (Figure 3b). Detection of InPd as the only intermetallic compound by HR-TEM is consistent with the obtained XRD results (Figure 2a).

During temperature-dependent MSR tests, the pre-treated material showed a very high CO_2-selectivity of 93% at 200 °C, increasing to 96% at 250 °C (Figure 4a), which is in agreement with literature.[16,26,29] Upon reaching 300 °C, the aerogel-based material outperforms previously investigated impregnated materials by a 50-times higher activity (50 mmol(H_2)/(mmol(Pd)×h)) as well as higher CO_2-selectivity (99% vs 97%).[26] Especially the excellent CO_2-selectivity is a major improvement compared to other systems (Figure S4), considering the aim of CO-levels <100 ppm. From the conversion at different temperatures during cooling and the second heating, an apparent activation energy of E_A = 142 kJ/mol was derived for the temperature range of 225 – 300 °C whereas in the range of 300 – 400 °C an apparent activation energy of E_A = 54 kJ/mol is obtained (Figure S2). The high-temperature activation energy is in the range of previously reported values for InPd[26,29,44], while the activation energy at low temperature is similar to the one of the In_2O_3-aerogel reference (Figure S3). This is a first hint of the presence of only In_2O_3 on the surface of the InPd/In_2O_3 aerogel below 300 °C. Since the subsequent isothermal section at 400 °C reveals a slow but continuous activity decrease by 25% from 300 mmol(H_2)/(mmol(Pd)×h) to 220 mmol(H_2)/(mmol(Pd)×h) over 20 h, the InPd/In_2O_3 aerogel was tested isothermally at 300 °C to investigate the long-term stability. Here, a significant initial increase in activity and selectivity is observed during the first 3 h (Figure 4b), indicating an increase of active surface species. After this initial period, a slow increase in activity and a slight decrease in CO_2-selectivity over the period of 60 h is observed. The final activity (50 mmol(H_2)/(mmol(Pd)×h), conversion 26%) is identical to the one obtained in the dynamic test, meaning that identical material changes were induced by MSR conditions.

Since In_2O_3 (conventional[45] as well as the aerogel in this study) shows CO_2-selectivities of 98% at 300 °C and 95% at 400 °C, compared to InPd/In_2O_3 with 99% and 93%, respectively,

a sole effect of In_2O_3 can be excluded as reason for the observed high CO_2-selectivity of the $InPd/In_2O_3$ aerogel at 300 °C. In addition, the support will not contribute significantly to the conversion at 300 °C due to its lower activity at 300 °C (10 mmol(H_2)/g(In_2O_3)×h), Figure S5 vs. 31 mmol(H_2)/g($InPd/In_2O_3$)×h), Figure S6) and the lower surface-specific activity[13].

To explore the nature of the known teamwork between intermetallic compounds and supporting oxide[18] and thus the role of the oxidic species in more detail, sequential MSR at 300 °C with unlabeled and ^{18}O-labeled water and methanol was conducted in the most selective state of the material (Figure 5). By injection of unlabeled reactants (**I**), reference signals for the different CO_2 species were obtained, which was followed by sequential ^{18}O-labeled (**II**) and unlabeled segments (**III**) to be able to ascribe the formation of $C^{16}O_2$ and $C^{18}O_2$, respectively, to oxygen from the previous segments contained in the material. Without participation of oxygen from the material, CO_2 will contain one oxygen atom from water and one from methanol. In the case of a Mars-van-Krevelen mechanism, an exchange of both oxygen atoms becomes possible. Upon switching to ^{18}O-labeled water and methanol (**II**), the initial formation of $C^{16}O_2$ reveals the participation of an oxidic species from the material in the reaction. This is likely In_2O_3 since its active role was proven in a similar reaction environment, i.e. the CO_2 hydrogenation.[46] $C^{18}O_2$ as well as the scrambled product $C^{16}O^{18}O$ are not formed instantly and a rise of the signal occurs with a delay. The absence of $C^{18}O_2$ in the beginning indicates that the intermetallic compound does not produce CO_2 without interaction with an oxidic species. The delay in the signal of $C^{16}O^{18}O$ can be understood by cleavage of C-O bonds during the reaction mechanism as reverse reaction of C-O bond formation, allowing the exchange of the oxygen originally contained in the methanol. This is in agreement with an H/D exchange observed for CO_2 hydrogenation intermediates on Cu/ZrO_2.[47] Since supporting indium oxide is not reduced under reaction conditions, in segment (**III**) a complete release of every ^{18}O-atom from In_2O_3 that replaced a ^{16}O-atom in segment (**II**) is expected. Switching back to unlabeled reactants (**III**) reveals narrower signals with a smaller area for $C^{18}O_2$ and $C^{16}O^{18}O$, not being identical to the shape of the signal curves for the phase with labeled water and methanol. From this it can be concluded that the supporting In_2O_3 as cause of the $C^{18}O_2$ formation is unlikely since this would produce equivalent signals for segment **II** and **III**. Thus, the main contribution of the observed different CO_2 species in all experiment phases is most likely caused by the $InPd/In_2O_3$ interface, in agreement with studies on Cu/Al_2O_3[48] and Cu/ZrO_2[47] in the CO_2 hydrogenation. Therefore, the slow decline of ^{16}O species in the labeled reactant phase is most likely linked to the incorporation of In_2O_3 into the already existing interface.

These isotope labeled experiments prove the active contribution of oxygen from the catalytic material during MSR in the form of a reactive InPd/In_2O_3 interface. This is strongly supported by *operando* studies on In-rich bulk InPd, where the formation of an InPd/In_3Pd_2/In_2O_3 surface structure was identified.[49] These results strongly suggest, that the intermetallic compound is not the active site, but apparently an active redox chemistry at the phase boundary of oxide and intermetallic compound is responsible for the high CO_2-selectivity of these catalytic materials and should be observable by the formation of different intermetallic compounds.

To investigate further the nature of the involved oxidic species, IR-spectroscopy was conducted (Figure S7). No remaining (hydroxy)carbonates could be detected after purging at 300 °C. Additional *operando* TG/MS measurements show parallel signal changes for H_2, m/z = 2, and CO_2, m/z = 44, during MSR conditions and purging, excluding a decomposition of hydrogen free CO_2 containing species, such as carbonates (Figure S8). These experiments show that either the concentration of (hydroxy)carbonates is extremely low or they are completely absent, making the impact of such species in the isotope labelled experiment neglectable.

XRD patterns of the material after 60 h at 300 °C reveal a small shoulder in the (110)-reflection of InPd at 39.3° and an additional reflection at 22.6°, corresponding to reflections of In_3Pd_2 (Figure 6). The formation of small amounts of In_3Pd_2 is ascribed to the reduction of In_2O_3 starting at around 300 °C (detected by TGA/MS) and an ongoing RMSI. It matches the indicated redox chemistry on the catalytic material during MSR by isotope labelled MSR. As expected, only In_3Pd_2 was detected in materials after dynamic and isothermal testing at 400 °C.

Upon exposure to MSR conditions at 250 °C, the InPd particles, which were observed after pre-reduction, are again identified by HR-TEM by comparison of their *d*-spacing in agreement with the literature (Figure 7).[16,26,29] At 300 °C surprisingly large particles with diameters up to >50 nm were observed. While no phase identification is possible (due to similar *d*-spacings of InPd and In_3Pd_2), a crystalline core and a roughly 2 nm thick partly crystalline shell with a lattice spacing of $d \approx 2.1$ Å are identified. Comparison of these results with the catalytic properties and XRD data leads to the conclusion that the initial InPd particles (96% selectivity at 250 °C) sinter to larger, indium-enriched mixed InPd/In_3Pd_2 particles at 300 °C. These possess higher selectivity (99% at 300 °C) while not showing an activity decrease upon sintering, indicating that the activity is not caused by the metallic particles alone, which is in agreement with the isotope labeled experiment. By High-angle annular dark field (HAADF)

micrographs and corresponding energy dispersive X-ray spectroscopy (EDX) maps (Figure 8) the high dispersion after exposure to 250 °C under MSR conditions is shown. Analysis of the large particles reveals a Pd-depleted surface, proving that at least a partial encapsulation of the intermetallic particles in In_2O_3 occurred in agreement with literature.[27]

No further changes are observed by HR-TEM (Figure S9 and Figure S10) or HAADF/EDX (Figure S11 and Figure S12) upon temperature changes. The observed partly crystalline shell probably results from the rapid size and compositional adjustment of the intermetallic In-Pd compounds to the reaction conditions at the particle surface and allows gas phase access to the intermetallic compound underneath while forming a static oxidic shell below 300 °C. While leading to deactivation at lower temperatures, the partly crystalline oxidic shell seemingly contributes to the unprecedented high CO_2-selectivity. The higher selectivity compared to previous studies on In-Pd materials might be related to different formation temperatures of this shell under reaction conditions.

The rapid sintering, the change in catalytic behavior, the isotope labelled experiments and thermodynamic calculations (data taken from references [52–55]) indicate, that the oxidic shell is not static, but more likely is caused by the highly dynamic RMSI of InPd and In_3Pd_2 with In_2O_3 reduction and formation at 300 °C. Thus, an equilibrium of partial reduction of In_2O_3 by CO (eq. 4), which is also supported by In-Pd/Al_2O_3 catalysts for NO_x removal[56], and a decomposition of the formed In_3Pd_2 by oxidation with water (eq. 5) is likely. Reduction of In_2O_3 can also occur by hydrogen but is thermodynamically not favored and will only happen locally when the H_2 concentration is increased due to the MSR. This dynamic equilibrium results in a high concentration of In_3Pd_2-InPd/In_2O_3 interface in contact with the gas phase, which either serves as active surface or allows spillover of adsorbed species.

$$4\ InPd + 3\ CO + In_2O_3 \rightleftharpoons 2\ In_3Pd_2 + 3\ CO_2 \qquad \Delta G_R^{300°C} = -1.89\ kJ/mol \qquad (4)$$

$$2\ In_3Pd_2 + 3\ H_2O \rightleftharpoons 4\ InPd + In_2O_3 + 3\ H_2 \qquad \Delta G_R^{300°C} = -51.50\ kJ/mol \qquad (5)$$

The thermodynamic stability of InPd at 250 °C under MSR conditions explains the stability against sintering and subsequent rapid sintering at 300 °C via the proposed equilibrium of two reactions. This equilibrium is most likely also responsible for the oxide layer formation, since indium diffuses from the original boundary over the complete particle due to alternating In_3Pd_2 formation and decomposition. In addition, the dynamic nature of the formed/reduced oxide results in a defective shell, which is an easily accessible source of oxygen upon reaching 300 °C under reaction conditions, supported by the active contribution of chemically bound oxygen

from the catalytic material. Oxygen incorporation from the catalytic material can happen at different pathways. One option is the oxidation of the side product CO. Another option is the promotion of the MSR pathway to CO_2 by formation of oxygen vacancies, which has been shown for the CO_2 hydrogenation.[57,58] However, the differentiation of the oxidation of formed CO or an enhancement of the MSR pathway, which does not include CO formation,[59] is not possible by our results. However, promotion of the MSR pathway by oxygen vacancies explains the increase of activity and selectivity in the first hours of the isothermal catalytic test, unlike CO oxidation (figure 4b). Both options do not exclude each other. For this reason, it is likely that the mentioned reactions (eq. 4 and 5) partly consume the formed CO and as consequence of this, oxygen vacancies are formed in the interface region, enhancing the activity and selectivity of the material. In this case the redox-activity of the material leads to the formation of more selective and active sites in the interface region. At 400 °C the oxidation of In_3Pd_2, despite being favorable ($\Delta G_R^{400°C}$ = -31.73 kJ/mol), is apparently not fast enough to provide sufficient amounts of In_2O_3 and/or oxygen vacancies in close proximity to InPd to either consume formed CO or sufficient promotion of the MSR pathway. This results in a lower CO_2-selectivity and the complete conversion of InPd into In_3Pd_2.

Conclusions

Pd/In_2O_3 aerogels were synthesized and subsequently transformed into intermetallic InPd with high specific surface area supported on an In_2O_3 aerogel by RMSI. A significant shift to lower reduction temperatures by 60 °C was accomplished for the formation of the intermetallic compound InPd compared to impregnated materials. Catalytic tests of the aerogel-based material revealed an unusually high CO_2-selectivity in MSR of 99% at 300 °C, accompanied by severe changes in the Pd distribution. Comparative catalytic investigation of $InPd/In_2O_3$, XRD and HR-TEM investigations revealed a temperature-dependent reactive phase change by RMSI and an active surface-oxide layer formation. ^{18}O-labeled MSR proofs the participation chemically bound oxygen in the catalytic material in MSR. Combining experimental results and thermodynamic considerations reveals teamwork between metallic and oxidic species as well as a high redox-activity responsible for the unprecedented CO_2-selectivity at 300 °C. At 250 °C and 400 °C this redox-activity is limited, leading to an encapsulation of the intermetallic compound or limited In_3Pd_2 oxidation, respectively. Both cases result in negative impacts on activity (encapsulation) or selectivity (lack of oxide or oxygen vacancies). Controlling the redox behavior is a key asset for highly active materials with exceptional selectivity in methanol steam reforming.

Supporting information

Experimental section, SEM micrograph of the as-prepared material, comparison of different catalytic materials, Arrhenius-plots, catalytic data of an In_2O_3 aerogel, ATR-IR spectrum of the material after catalysis, *operando* TGA/MS, additional HR-TEM, -STEM, -EDX micrographs

Acknowledgement

The European Integrated Centre for the Development of New Metallic Alloys and Compounds (ECMetAC) is thankfully acknowledged for funding Nicolas Köwitsch a Young Scientist Exchange for HR-TEM investigations.

The Deutsche Bundesstiftung Umwelt is acknowledged for the financial support of the work of Lukas Thoni. Acknowledged is also the financial support, which has been received by the ERC AdG AEROCAT.

Isabel Köwitsch acknowledges the financial support from the European Social Fund (ESF, Project No.100 327 773) for her PhD scholarship.

References

(1) Asinger, F. *Methanol — Chemie- und Energierohstoff*, 1st ed.; Springer-Verlag: Berlin, Heidelberg, **1986**, 57-267. https://doi.org/10.1007/978-3-642-70763-6.

(2) Olah, G. A. Beyond Oil and Gas: The Methanol Economy. *Angew. Chemie Int. Ed.* **2005**, *44* (18), 2636–2639. https://doi.org/10.1002/anie.200462121.

(3) Oetjen, H.-F.; Schmidt, V. M.; Stimming, U.; Trila, F. Performance Data of a Proton Exchange Membrane Fuel Cell Using H_2/CO as Fuel Gas. *J. Electrochem. Soc.* **1996**, *143* (12), 3838–3842. https://doi.org/10.1149/1.1837305.

(4) Sá, S.; Silva, H.; Brandão, L.; Sousa, J. M.; Mendes, A. Catalysts for methanol steam reforming—A review. *Appl. Catal. B Environ.* **2010**, *99* (1–2), 43–57. https://doi.org/10.1016/j.apcatb.2010.06.015.

(5) Peppley, B. A.; Amphlett, J. C.; Kearns, L. M.; Mann, R. F. Methanol–steam reforming on Cu/ZnO/Al_2O_3. Part 1: the reaction network. *Appl. Catal. A Gen.* **1999**, *179* (1), 21–29. https://doi.org/https://doi.org/10.1016/S0926-860X(98)00298-1.

(6) Purnama, H.; Girgsdies, F.; Ressler, T.; Schattka, J. H.; Caruso, R. A.; Schomäcker, R.; Schlögl, R. Activity and selectivity of a nanostructured CuO/ZrO_2 catalyst in the steam reforming of methanol. *Catal. Letters* **2004**, *94* (1/2), 61–68. https://doi.org/10.1023/B:CATL.0000019332.80287.6b.

(7) Shen, G.-C.; Fujita, S.; Matsumoto, S.; Takezawa, N. Steam reforming of methanol on binary Cu/ZnO catalysts: Effects of preparation condition upon precursors, surface structure and catalytic activity. *J. Mol. Catal. A Chem.* **1997**, *124* (2–3), 123–136. https://doi.org/10.1016/S1381-1169(97)00078-2.

(8) Iwasa, N.; Mayanagi, T.; Ogawa, N.; Sakata, K.; Takezawa, N. New catalytic functions of Pd-Zn, Pd-Ga, Pd-In, Pt-Zn, Pt-Ga and Pt-In alloys in the conversions of methanol. *Catal. Letters* **1998**, *54* (3), 119–123. https://doi.org/10.1023/A:1019056728333.

(9) Liu, X.; Men, Y.; Wang, J.; He, R.; Wang, Y. Remarkable support effect on the reactivity of $Pt/In_2O_3/MO_x$ catalysts for methanol steam reforming. *J. Power Sources* **2017**, *364*, 341–350. https://doi.org/10.1016/J.JPOWSOUR.2017.08.043.

(10) Armbrüster, M.; Behrens, M.; Föttinger, K.; Friedrich, M.; Gaudry, É.; Matam, S. K.; Sharma, H. R. The Intermetallic Compound ZnPd and Its Role in Methanol Steam Reforming. *Catal. Rev. Sci. Eng.* **2013**, *55* (3), 289–367. https://doi.org/10.1080/01614940.2013.796192.

(11) Li, X.; Li, L.; Lin, J.; Qiao, B.; Yang, X.; Wang, A.; Wang, X. Reactivity of Methanol Steam Reforming on ZnPd Intermetallic Catalyst: Understanding from Microcalorimetric and FT-IR Studies. *J. Phys. Chem. C* **2018**, *122* (23), 12395–12403. https://doi.org/10.1021/acs.jpcc.8b03933.

(12) Föttinger, K. The effect of CO on intermetallic PdZn/ZnO and Pd_2Ga/Ga_2O_3 methanol steam reforming catalysts: A comparative study. *Catal. Today* **2013**, *208*, 106–112. https://doi.org/10.1016/j.cattod.2012.12.004.

(13) Lorenz, H.; Rameshan, C.; Bielz, T.; Memmel, N.; Stadlmayr, W.; Mayr, L.; Zhao, Q.; Soisuwan, S.; Klötzer, B.; Penner, S. From Oxide-Supported Palladium to Intermetallic Palladium Phases: Consequences for Methanol Steam Reforming. *ChemCatChem* **2013**, *5* (6), 1273–1285. https://doi.org/10.1002/cctc.201200712.

(14) Iwasa, N.; Takezawa, N. New supported Pd and Pt alloy catalyst for steam reforming and dehydrogenation of methanol. *Top. Catal.* **2003**, *22* (3–4), 215–224. https://doi.org/10.1023/A:1023571819211.

(15) Penner, S.; Armbrüster, M. Formation of Intermetallic Compounds by Reactive Metal-Support Interaction: A Frequently Encountered Phenomenon in Catalysis.

ChemCatChem **2015**, *7* (3), 374–392. https://doi.org/10.1002/cctc.201402635.

(16) Iwasa, N.; Takezawa, N. New supported Pd and Pt alloy catalysts for steam reforming and dehydrogenation of methanol. *Top. Catal.* **2003**, *22* (3–4), 215–224. https://doi.org/10.1023/A:1023571819211.

(17) Friedrich, M.; Teschner, D.; Knop-Gericke, A.; Armbrüster, M. Influence of bulk composition of the intermetallic compound ZnPd on surface composition and methanol steam reforming properties. *J. Catal.* **2012**, *285* (1), 41–47. https://doi.org/10.1016/j.jcat.2011.09.013.

(18) Friedrich, M.; Penner, S.; Heggen, M.; Armbrüster, M. High CO_2 Selectivity in Methanol Steam Reforming through ZnPd/ZnO Teamwork. *Angew. Chemie Int. Ed.* **2013**, *52* (16), 4389–4392. https://doi.org/10.1002/anie.201209587.

(19) Heggen, M.; Penner, S.; Friedrich, M.; Dunin-Borkowski, R. E.; Armbrüster, M. Formation of ZnO Patches on ZnPd/ZnO during Methanol Steam Reforming: A Strong Metal-Support Interaction Effect? *J. Phys. Chem. C* **2016**, *120* (19), 10460–10465. https://doi.org/10.1021/acs.jpcc.6b02562.

(20) Eblagon, K. M.; Concepción, P. H.; Silva, H.; Mendes, A. Ultraselective low temperature steam reforming of methanol over PdZn/ZnO catalysts-Influence of induced support defects on catalytic performance. *Appl. Catal. B Environ.* **2014**, *154–155*, 316–328. https://doi.org/10.1016/j.apcatb.2014.02.032.

(21) Haghofer, A.; Ferri, D.; Föttinger, K.; Rupprechter, G. Who is doing the job? Unraveling the role of Ga_2O_3 in methanol steam reforming on Pd_2Ga/Ga_2O_3. *ACS Catal.* **2012**, *2* (11), 2305–2315. https://doi.org/10.1021/cs300480c.

(22) Fricke, J.; Emmerling, A. Aerogels. *J. Am. Ceram. Soc.* **1992**, *75* (8), 2027–2035. https://doi.org/10.1111/j.1151-2916.1992.tb04461.x.

(23) Rechberger, F.; Niederberger, M. Synthesis of Aerogels: From Molecular Routes to 3-Dimensional Nanoparticle Assembly. *Nanoscale Horizons* **2017**, *2* (2), 1–66. https://doi.org/10.1039/C6NH00077K.

(24) Ziegler, C.; Wolf, A.; Liu, W.; Herrmann, A.-K.; Gaponik, N.; Eychmüller, A. Modern Inorganic Aerogels. *Angew. Chemie Int. Ed.* **2017**, *56*, 13200–13221. https://doi.org/10.1002/anie.201611552.

(25) Ziegler, C.; Klosz, S.; Borchardt, L.; Oschatz, M.; Kaskel, S.; Friedrich, M.; Kriegel,

R.; Keilhauer, T.; Armbrüster, M.; Eychmüller, A. ZnPd/ZnO Aerogels as Potential Catalytic Materials. *Adv. Funct. Mater.* **2016**, *26* (7), 1014–1020. https://doi.org/10.1002/adfm.201503000.

(26) Neumann, M.; Teschner, D.; Knop-Gericke, A.; Reschetilowski, W.; Armbrüster, M. Controlled synthesis and catalytic properties of supported In-Pd intermetallic compounds. *J. Catal.* **2016**, *340*, 49–59. https://doi.org/10.1016/j.jcat.2016.05.006.

(27) Rameshan, C.; Lorenz, H.; Armbrüster, M.; Kasatkin, I.; Klötzer, B.; Götsch, T.; Ploner, K.; Penner, S. Impregnated and Co-precipitated Pd–Ga_2O_3, Pd–In_2O_3 and Pd–Ga_2O_3–In_2O_3 Catalysts: Influence of the Microstructure on the CO_2 Selectivity in Methanol Steam Reforming. *Catal. Letters* **2018**, *148* (10), 3062–3071. https://doi.org/10.1007/s10562-018-2491-4.

(28) Men, Y.; Kolb, G.; Zapf, R.; O'Connell, M.; Ziogas, A. Methanol steam reforming over bimetallic Pd-In/Al_2O_3 catalysts in a microstructured reactor. *Appl. Catal. A Gen.* **2010**, *380* (1–2), 15–20. https://doi.org/10.1016/j.apcata.2010.03.004.

(29) Lorenz, H.; Turner, S.; Lebedev, O. I.; Van Tendeloo, G.; Klötzer, B.; Rameshan, C.; Pfaller, K.; Penner, S. Pd-In_2O_3 interaction due to reduction in hydrogen: Consequences for methanol steam reforming. *Appl. Catal. A Gen.* **2010**, *374* (1–2), 180–188. https://doi.org/10.1016/j.apcata.2009.12.007.

(30) García-Trenco, A.; Regoutz, A.; White, E. R.; Payne, D. J.; Shaffer, M. S. P.; Williams, C. K. PdIn intermetallic nanoparticles for the Hydrogenation of CO_2 to Methanol. *Appl. Catal. B Environ.* **2018**, *220*, 9–18. https://doi.org/10.1016/J.APCATB.2017.07.069.

(31) Snider, J. L.; Streibel, V.; Hubert, M. A.; Choksi, T. S.; Valle, E.; Upham, D. C.; Schumann, J.; Duyar, M. S.; Gallo, A.; Abild-Pedersen, F.; Jaramillo, T. F. Revealing the Synergy between Oxide and Alloy Phases on the Performance of Bimetallic In–Pd Catalysts for CO_2 Hydrogenation to Methanol. *ACS Catal.* **2019**, *9* (4), 3399–3412. https://doi.org/10.1021/acscatal.8b04848.

(32) Wu, Z.; Wegener, E. C.; Tseng, H.-T.; Gallagher, J. R.; Harris, J. W.; Diaz, R. E.; Ren, Y.; Ribeiro, F. H.; Miller, J. T. Pd–In intermetallic alloy nanoparticles: highly selective ethane dehydrogenation catalysts. *Catal. Sci. Technol.* **2016**, *6* (18), 6965–6976. https://doi.org/10.1039/C6CY00491A.

(33) Burueva, D. B.; Kovtunov, K. V.; Bukhtiyarov, A. V.; Barskiy, D. A.; Prosvirin, I. P.; Mashkovsky, I. S.; Baeva, G. N.; Bukhtiyarov, V. I.; Stakheev, A. Y.; Koptyug, I. V. Selective Single-Site Pd−In Hydrogenation Catalyst for Production of Enhanced Magnetic Resonance Signals Using Parahydrogen. *Chem. - A Eur. J.* **2018**, *24* (11), 2547–2553. https://doi.org/10.1002/chem.201705644.

(34) Markov, P. V.; Bragina, G. O.; Baeva, G. N.; Tkachenko, O. P.; Mashkovskii, I. S.; Yakushev, I. A.; Vargaftik, M. N.; Stakheev, A. Y. Supported catalysts based on Pd–In nanoparticles for the liquid-phase hydrogenation of terminal and internal alkynes: 1. formation and structure. *Kinet. Catal.* **2016**, *57* (5), 617–624. https://doi.org/10.1134/S002315841605013X.

(35) Cao, Y.; Sui, Z.; Zhu, Y.; Zhou, X.; Chen, D. Selective Hydrogenation of Acetylene over Pd-In/Al_2O_3 Catalyst: Promotional Effect of Indium and Composition-Dependent Performance. *ACS Catal.* **2017**, *7* (11), 7835–7846. https://doi.org/10.1021/acscatal.7b01745.

(36) Gash, A. E.; Tillotson, T. M.; Satcher, J. H.; Hrubesh, L. W.; Simpson, R. L. New Sol-Gel Synthetic Route to Transition and Main-Group Metal Oxide Aerogels Using Inorganic Salt Precursors. *J. Non. Cryst. Solids* **2001**, *285* (1–3), 22–28. https://doi.org/10.1016/S0022-3093(01)00427-6.

(37) Gash, A. E.; Tillotson, T. M.; Satcher, J. H.; Poco, J. F.; Hrubesh, L. W.; Simpson, R. L. Use of Epoxides in the Sol-Gel Synthesis of Porous Iron(III) Oxide Monoliths from Fe(III) Salts. *Chem. Mater.* **2001**, *13* (3), 999–1007. https://doi.org/10.1021/cm0007611.

(38) Ambrosini, A.; Duarte, A.; Poeppelmeier, K. R.; Lane, M.; Kannewurf, C. R.; Mason, T. O. Electrical, Optical, and Structural Properties of Tin-Doped In_2O_3-M_2O_3 Solid Solutions (M = Y, Sc). *J. Solid State Chem.* **2000**, *153*, 41–47. https://doi.org/10.1006/jssc.2000.8737.

(39) Paiz, J.; Fitch, J.; Peterson, E.; Hough, T.; Barnard, W.; Datye, A. Synthesis of PdO-ZnO Mixed Oxide Precursors for PdZn Intermetallic Catalysts. *Cryst. Res. Technol.* **2014**, *49* (9), 699–707. https://doi.org/10.1002/crat.201400070.

(40) Baba, K.; Miyagawa, U.; Watanabe, K.; Sakamoto, Y.; Flanagan, T. B. Electrical Resistivity Changes Due to Interstitial Hydrogen in Palladium-Rich Substitutional Alloys. *J. Mater. Sci.* **1990**, *25* (9), 3910–3916. https://doi.org/10.1007/BF00582459.

(41) Mullica, D. F.; Beall, G. W.; Milligan, W. O.; Korp, J. D.; Bernal, I. THE CRYSTAL STRUCTURE OF CUBIC $In(OH)_3$ BY X-RAY AND NEUTRON DIFFRACTION METHODS. *J. Inorg. Nucl. Chem.* **1979**, *41* (3), 277–282. https://doi.org/10.1016/0022-1902(79)80133-5.

(42) Christensen, A. N.; Grønbæk, R.; Rasmussen, S. E. The Crystal Structure of InOOH. *Acta Chem. Scand.* **1964**, *18*, 1261–1266. https://doi.org/10.3891/acta.chem.scand.18-1261.

(43) McGuirk, G. M.; Ledieu, J.; Gaudry, É.; De Weerd, M. C.; Fournée, V. Surface Structures of In-Pd Intermetallic Compounds. I. Experimental Study of in Thin Films on Pd(111) and Alloy Formation. *J. Chem. Phys.* **2014**, *141* (8), 084702. https://doi.org/10.1063/1.4892408.

(44) Rameshan, C.; Lorenz, H.; Mayr, L.; Penner, S.; Zemlyanov, D.; Arrigo, R.; Haevecker, M.; Blume, R.; Knop-Gericke, A.; Schlögl, R.; Klötzer, B. CO_2-selective methanol steam reforming on In-doped Pd studied by in situ X-ray photoelectron spectroscopy. *J. Catal.* **2012**, *295*, 186–194. https://doi.org/10.1016/j.jcat.2012.08.008.

(45) Lorenz, H.; Jochum, W.; Klötzer, B.; Stöger-Pollach, M.; Schwarz, S.; Pfaller, K.; Penner, S. Novel methanol steam reforming activity and selectivity of pure In_2O_3. *Appl. Catal. A Gen.* **2008**, *347* (1), 34–42. https://doi.org/10.1016/j.apcata.2008.05.028.

(46) Tsoukalou, A.; Abdala, P. M.; Stoian, D.; Huang, X.; Willinger, M.-G.; Fedorov, A.; Müller, C. R. Structural Evolution and Dynamics of an In_2O_3 Catalyst for CO_2 Hydrogenation to Methanol: An Operando XAS-XRD and In Situ TEM Study. *J. Am. Chem. Soc.* **2019**, *141*, 13497–13505. https://doi.org/10.1021/jacs.9b04873.

(47) Larmier, K.; Liao, W. C.; Tada, S.; Lam, E.; Verel, R.; Bansode, A.; Urakawa, A.; Comas-Vives, A.; Copéret, C. CO_2-to-Methanol Hydrogenation on Zirconia-Supported Copper Nanoparticles: Reaction Intermediates and the Role of the Metal–Support Interface. *Angew. Chemie - Int. Ed.* **2017**, *56* (9), 2318–2323. https://doi.org/10.1002/anie.201610166.

(48) Lam, E.; Corral-Pérez, J. J.; Larmier, K.; Noh, G.; Wolf, P.; Comas-Vives, A.; Urakawa, A.; Copéret, C. CO_2 Hydrogenation on Cu/Al_2O_3: Role of the Metal/Support Interface in Driving Activity and Selectivity of a Bifunctional Catalyst. *Angew. Chemie - Int. Ed.* **2019**, *58* (39), 13989–13996.

https://doi.org/10.1002/anie.201908060.

(49) Ivarsson, D. C. A.; Neumann, M.; Levin, A. A.; Keilhauer, T.; Wochner, P.; Armbrüster, M. In Operando GIXRD and XRR on Polycrystalline $In_{52}Pd_{48}$. *Zeitschrift fur Anorg. und Allg. Chemie* **2014**, *640* (15), 3065–3069. https://doi.org/10.1002/zaac.201400223.

(50) Flandorfer, H. Phase Relationships in the In-Rich Part of the In-Pd System. *J. Alloys Compd.* **2002**, *336* (1–2), 176–180. https://doi.org/10.1016/S0925-8388(01)01859-X.

(51) He, J. L.; Shen, Z. Q.; Wu, E.; Liu, Z. Y.; He, L. L.; Yu, D. L.; Guo, L. C.; Wu, Q. H.; Luo, X. G.; Hu, Q. K.; Li, D. C.; Yanagisawa, O.; Tian, Y. J. Carbon-rich boron carbide in the eutectic product synthesized by resistance heating of B_2CN in graphite. *J. Alloys Compd.* **2007**, *437* (1–2), 238–246. https://doi.org/10.1016/j.jallcom.2006.07.097.

(52) Binnewies, M.; Milke, E. *Thermochemical Data of Elements and Compounds*; WILEY-VCH Verlag: Weinheim, **2002**, 630-795.

(53) Bird, J. M.; Bryant, A. W.; Pratt, J. N. Thermodynamic Properties of Palladium + Indium Alloys: Solid Electrolyte Cell and Differential Scanning Calorimetry Studies. *J. Chem. Thermodyn.* **1975**, *7* (6), 577–586. https://doi.org/10.1016/0021-9614(75)90192-5.

(54) Amore, S.; Delsante, S.; Parodi, N.; Borzone, G. Thermochemistry of Pd–In, Pd–Sn and Pd–Zn Alloy Systems. *Thermochim. Acta* **2008**, *481* (1–2), 1–6. https://doi.org/10.1016/j.tca.2008.09.018.

(55) Perring, L.; Kuntz, J. J.; Bussy, F.; Gachon, J. C. Heat Capacity Measurements by Differential Scanning Calorimetry in the Pd-Pb, Pd-Sn and Pd-In Systems. *Thermochim. Acta* **2001**, *366* (1), 31–36. https://doi.org/10.1016/S0040-6031(00)00731-0.

(56) Jeon, J.; Ham, H.; Xing, F.; Nakaya, Y.; Shimizu, K.; Furukawa, S. PdIn-Based Pseudo-Binary Alloy as a Catalyst for NO_x Removal under Lean Conditions. *ACS Catal.* **2020**, *10* (19), 11380–11384. https://doi.org/10.1021/acscatal.0c03427.

(57) Martin, O.; Martín, A. J.; Mondelli, C.; Mitchell, S.; Segawa, T. F.; Hauert, R.; Drouilly, C.; Curulla-Ferré, D.; Pérez-Ramírez, J. Indium Oxide as a Superior Catalyst for Methanol Synthesis by CO_2 Hydrogenation. *Angew. Chemie Int. Ed.* **2016**, *55* (21),

6261–6265. https://doi.org/10.1002/anie.201600943.

(58) Manrique, R.; Rodríguez-Pereira, J.; Rincón-Ortiz, S. A.; Bravo-Suárez, J. J.; Baldovino-Medrano, V. G.; Jiménez, R.; Karelovic, A. The nature of the active sites of Pd–Ga catalysts in the hydrogenation of CO_2 to methanol. *Catal. Sci. Technol.* **2020**, 6644–6658. https://doi.org/10.1039/d0cy00956c.

(59) Lin, S.; Xie, D.; Guo, H. Pathways of Methanol Steam Reforming on PdZn and Comparison with Cu. *J. Phys. Chem. C* **2011**, *115* (42), 20583–20589. https://doi.org/10.1021/jp206511q.

Figures

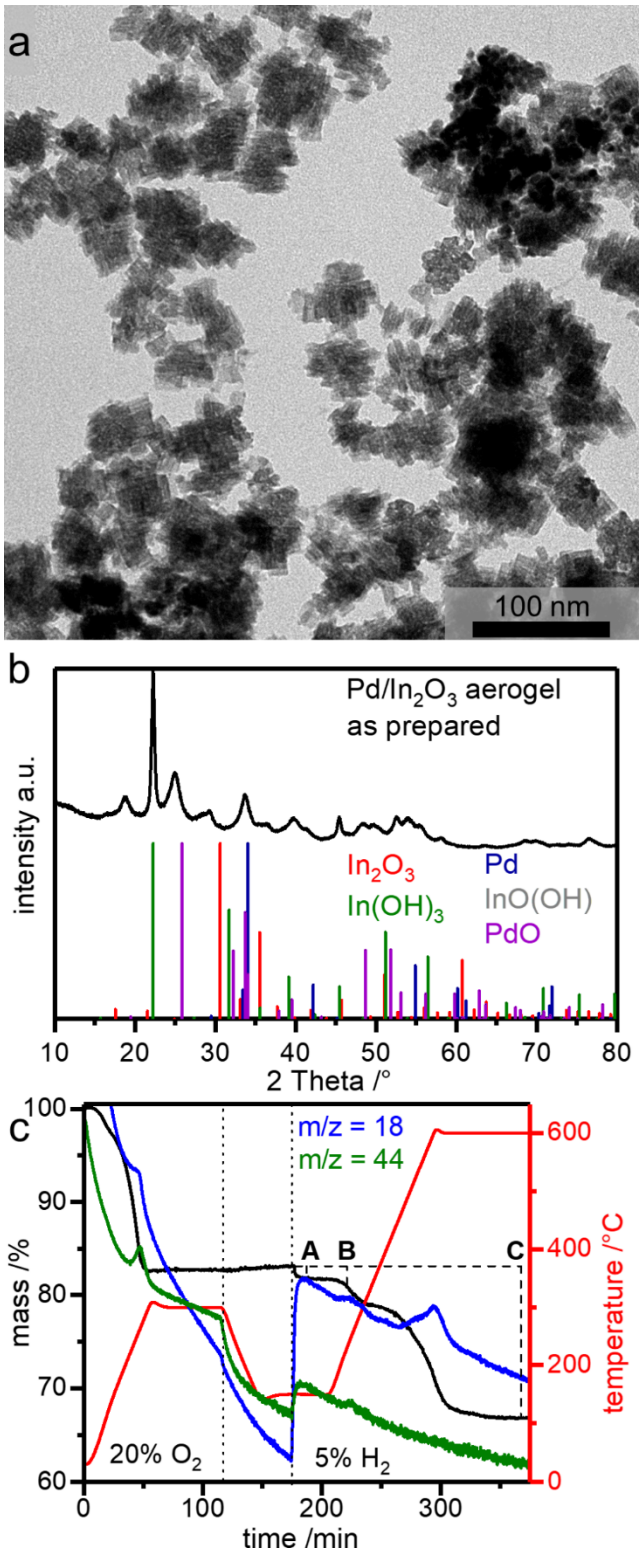

Figure 1: a) TEM micrograph of the as-prepared aerogel, revealing a network structure consisting of polycrystalline secondary particles. b) XRD pattern of the as-prepared aerogel with the calculated patterns of In_2O_3[38], PdO[39], Pd[40] $In(OH)_3$[41] and InO(OH)[42]. c) TGA/MS measurement of the as-prepared Pd/In_2O_3 aerogel along with the ion current for the fragments m/z = 18 as indicator for water and m/z = 44 as indicator for CO_2.

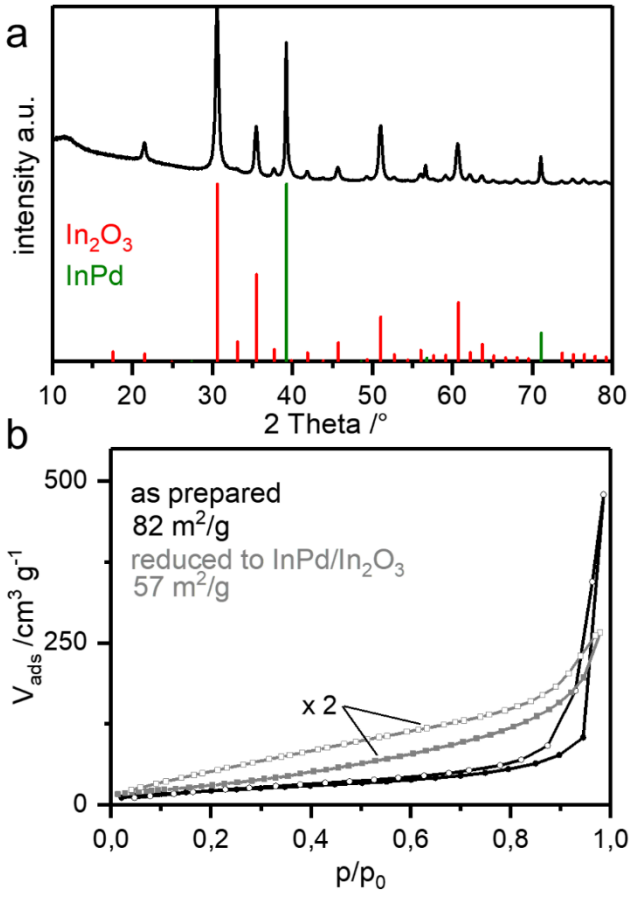

Figure 2: a) XRD pattern of the InPd/In_2O_3 aerogel reduced at 230 °C. Additionally shown are the calculated patterns of In_2O_3[38] and InPd[43]. b) Nitrogen physisorption measurements of the aerogel before and after thermal treatment. Both materials show type II isotherms and a decrease of the specific surface area upon pre-treatment is observed. Empty symbols belong to the desorption curves.

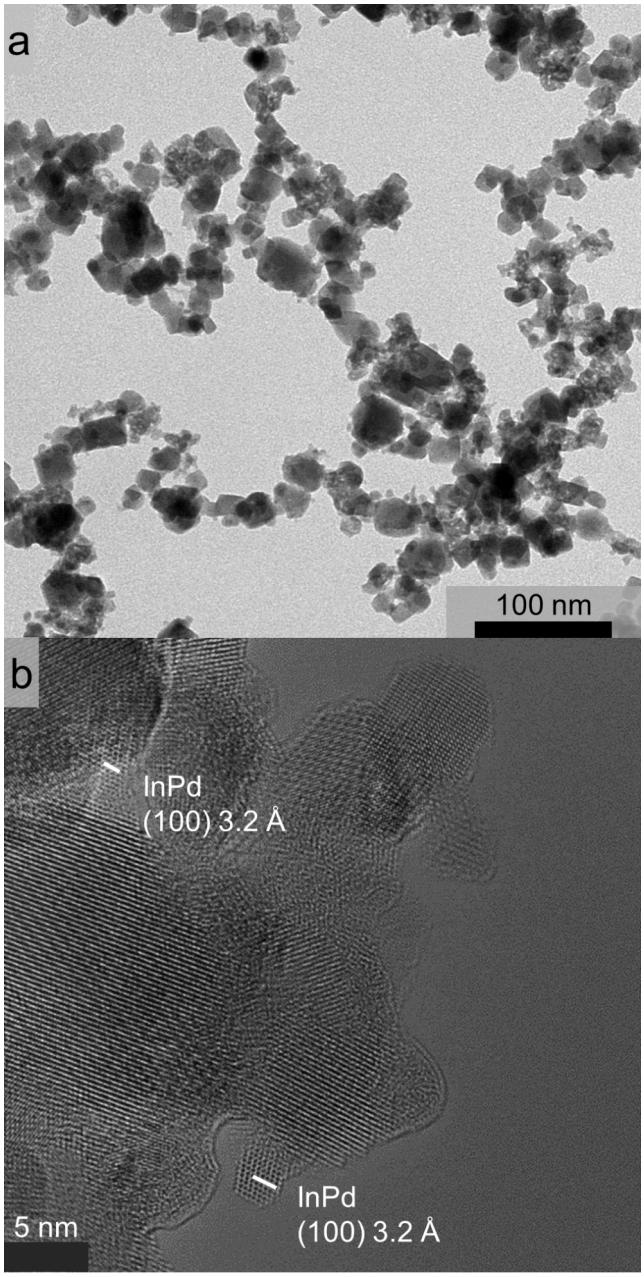

Figure 3: a) TEM micrograph and b) HR-TEM micrograph of the material pre-reduced at 230 °C. b) A ripened network structure is detected and InPd nanoparticles with < 10 nm diameter were identified by their (100)-spacing.

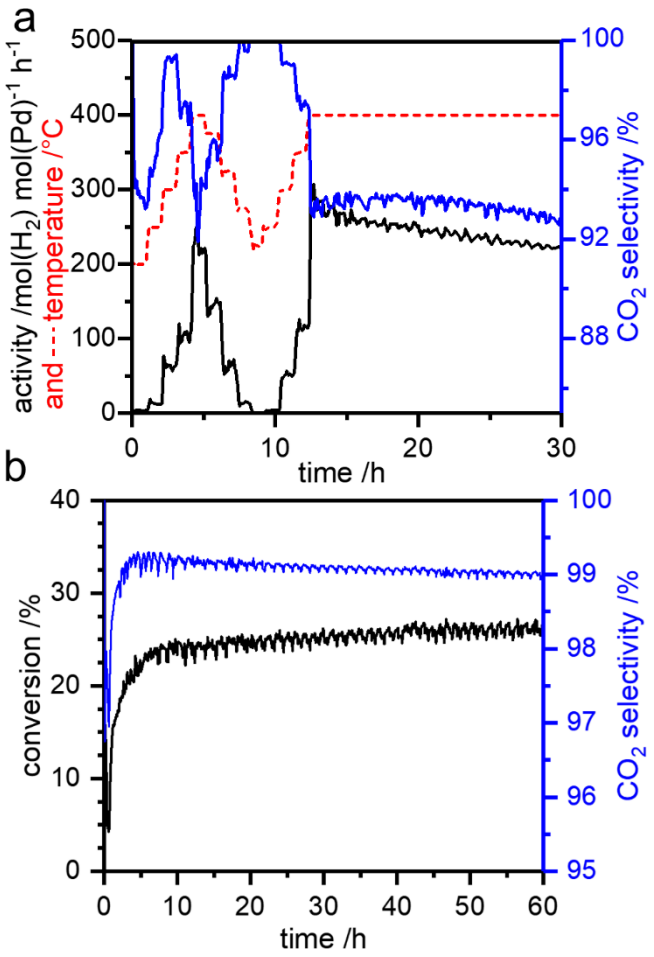

Figure 4: Catalytic properties of InPd/In_2O_3 (300 $mg_{catalyst}$) in MSR. a) Test under dynamic temperature conditions revealing altered properties regarding selectivity upon reaching 300 °C and slightly decreasing activity after 20 h at 400 °C. Temperature and activity share the same numerical values b) Isothermal test at 300 °C (1000 $mg_{catalyst}$) revealing an initial rise in activity and selectivity.

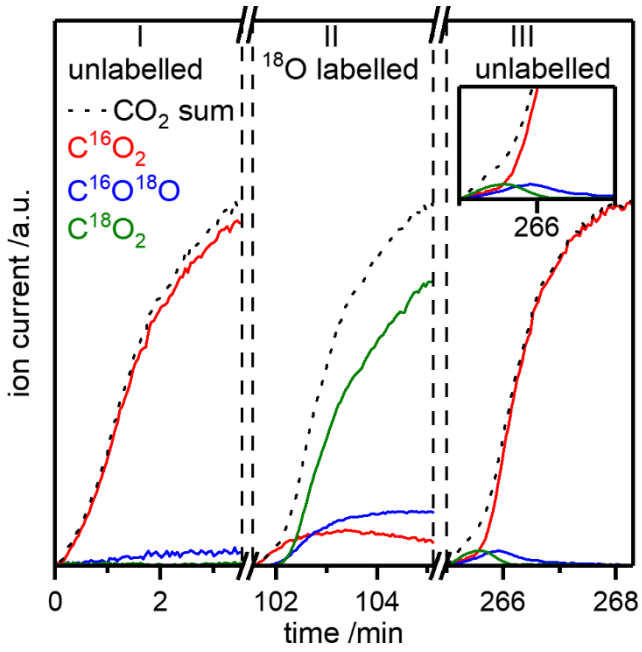

Figure 5: MS-signals for CO_2 with different oxygen isotopes during the initial contact of catalyst and reactant stream. Experimental order was unlabeled reactants, ^{18}O-labeled reactants and unlabeled reactants after thoroughly purging with inert gas between every vapor composition. Dotted line represents the sum of the different CO_2 species.

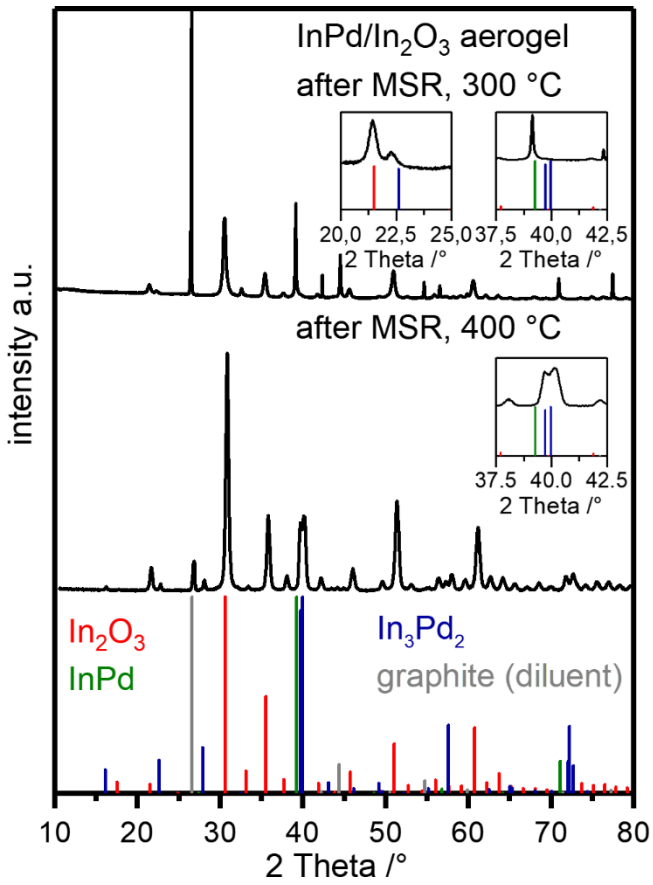

Figure 6: XRD patterns of the InPd/In_2O_3 aerogel after MSR at 300 °C (top) and after MSR at 400 °C (bottom). The insets show the magnified reflections in the shown 2 Theta range. Additionally shown are the calculated patterns of In_2O_3[38], InPd[43], In_3Pd_2[50] and graphite[51]. The graphite reflections after catalysis are caused by graphite used to dilute the active material.

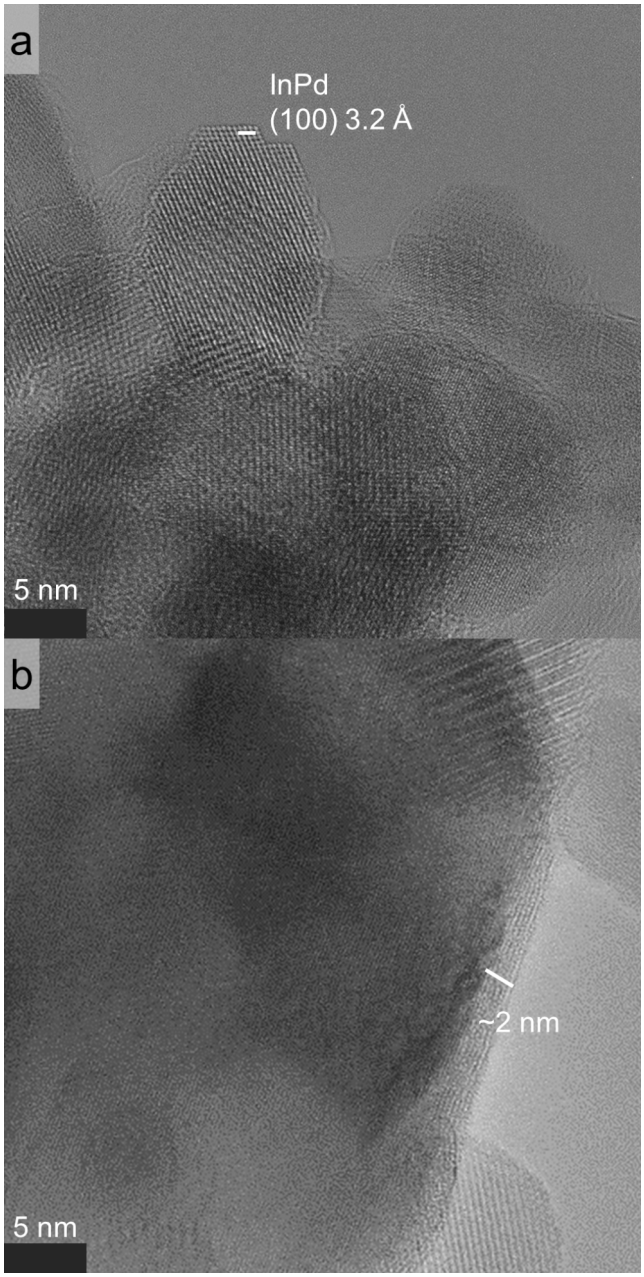

Figure 7: HR-TEM micrographs of a) the material after MSR conditions at 250 °C and b) after MSR conditions at 300 °C. In the first state small InPd nanoparticles with < 10 nm diameter were identified by the (100) spacing. After 300 °C under MSR conditions newly formed particles with up to 200 nm diameter are observed. Those particles exhibit a ~ 2 nm thick partly crystalline shell.

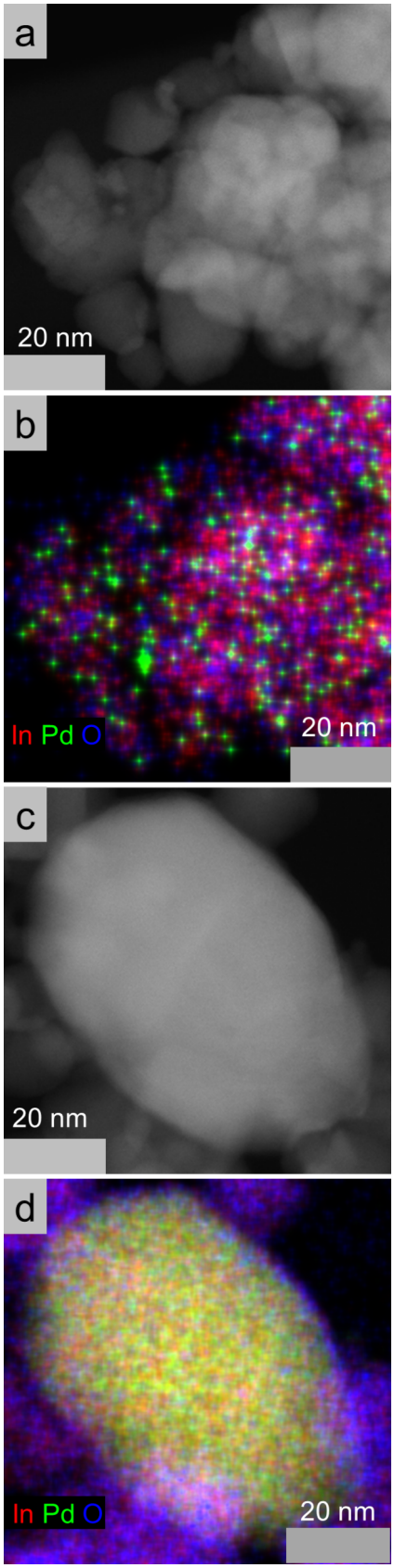

Figure 8: HAADF (a, c) and EDX (b, d) micrographs of the InPd/In_2O_3 aerogel at different stages of catalysis. a) and b) are representative images of the sample after being heated to 250 °C under MSR conditions. c) and d) are representative images of Pd containing particles after the sampled was heated to 300 °C under MSR conditions.

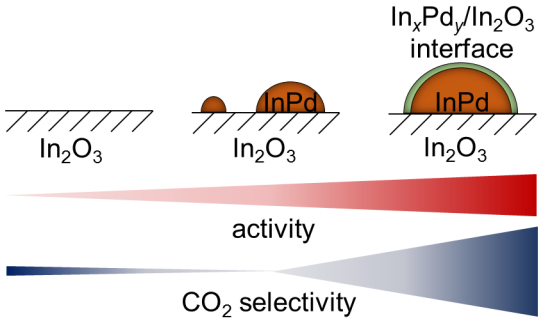

Table of content figure: ***Different active In_xPd_y/In_2O_3 species*** *in methanol steam reforming have been identified. The dynamic In_xPd_y/In_2O_3 interface has been proven more active and selective than In_2O_3 or InPd by contribution of oxygen in the catalytic material to the reaction in the interface region.*